GEOPHYSICS, VOL. 83, NO. 5 (SEPTEMBER-OCTOBER 2018); P. S409–S419, 14 FIGS.
10.1190/GEO2017-0646.1

A practical implementation of subsalt Marchenko imaging with a Gulf of Mexico data set

Xueyi Jia[1], Antoine Guitton[1], and Roel Snieder[1]

ABSTRACT

Marchenko redatuming allows one to use surface seismic reflection data to generate the seismic response from sources at the surface to any point in the subsurface. Without requiring much information about the earth's properties, the seismic response generated by Marchenko redatuming contains accurate estimates of not only the primaries but also the internal multiples. A target-oriented imaging method, referred to as Marchenko imaging, was implemented for imaging complex structures of the earth using the seismic response obtained through Marchenko redatuming. Taking account of the contribution of primaries and internal multiples, Marchenko imaging produces images that contain fewer artifacts than the images obtained using conventional imaging methods (e.g., reverse time migration) with the same input data. In this study, we applied Marchenko imaging to a field data set acquired at the Gulf of Mexico to produce an image of a subsalt area. We investigated two important and practical aspects of the Marchenko framework: (1) the missing near offsets in marine shot records and (2) the calibration of the reflection data. Finally, we suggested a workflow for processing the marine towed-streamer field data set acquired at the Gulf of Mexico, and we have developed a complete theoretical and practical framework to produce a target-oriented subsalt image using the Marchenko methods. The images obtained from Marchenko imaging are consistent and comparable, for the most part, with conventional migration methods. However, Marchenko imaging achieves improvements in the continuity of the geologic structures and in suppressing the artifacts that are caused by internal multiples.

INTRODUCTION

Marchenko imaging is a technique used to image the subsurface of the earth using the primaries and multiples of seismic data, and it aims to produce an image that is free of artifacts caused by multiple reflections. This imaging approach is based on the redatumed reflection response created by a method referred to as Marchenko redatuming, which virtually moves the surface seismic sources and receivers to a deeper depth, close to the targets in the medium. Significantly, the redatumed data contain only the reflection response below the redatuming depth, and the medium above is treated as reflection free. Therefore, Marchenko imaging provides a target-oriented solution specifically for imaging the area below complex structures such as salt bodies (which can create strong multiples).

Marchenko redatuming (the core of the Marchenko framework) contains two steps: receiver redatuming and source redatuming (Figure 1). Receiver redatuming aims to retrieve wavefields from sources at the surface to a virtual receiver in the medium using Marchenko-type equations. Classic redatuming methods (Berryhill, 1979, 1984; Kinneging et al., 1989) do not account for internal multiple reflections; hence, spurious events can emerge when there is only single-sided illumination (Snieder et al., 2006). With Marchenko redatuming, the primaries and the multiples can be correctly estimated (Rose, 2002; Broggini et al., 2012; Wapenaar et al., 2014b) and the retrieved wavefields are naturally separated into up- and downgoing components. In the second step of source redatuming, these up- and downgoing wavefields can be used to move the sources to the redatuming level by approaches such as multidimensional deconvolution (MDD) (van der Neut et al., 2011). Unlike the wavefield retrieval method that uses seismic interferometry, which requires the data recorded at a physical receiver in the subsurface (Bakulin and Calvert, 2006), Marchenko redatuming requires only surface seismic data and a background velocity model as inputs, which are the same requirements for many standard imaging

Manuscript received by the Editor 1 October 2017; revised manuscript received 17 March 2018; published ahead of production 09 June 2018; published online 07 August 2018.
[1]Colorado School of Mines, Center for Wave Phenomena, Golden, Colorado, USA. E-mail: jia@mines.edu; aguitton@gmail.com; rsnieder@mines.edu.

techniques (e.g., reverse time migration [RTM]). A background velocity model, instead of being used to perform any wavefield propagation, is used to compute the traveltime of the first arrival from a subsurface point to the surface. In general, the Marchenko redatuming process does not require any more details of the medium parameters than conventional imaging schemes (Broggini et al., 2014).

Broggini and Snieder (2012) first show the scheme to use Marchenko equations to retrieve the Green's functions between an arbitrary virtual source position inside the 1D medium and a receiver at the surface with only the reflection response recorded at the surface of that medium. Wapenaar et al. (2014a, 2014b) then derive the 3D Marchenko equations, which relate the single-sided reflection response of a 3D medium to a focusing wavefield, of which the focusing point is defined by estimating the traveltime from this point to the surface.

Marchenko redatuming has been extended to elastic media using P- and S-wave measured potentials from P- and S-wave potential sources (Wapenaar, 2014) and using velocity-stress recordings from force and deformation sources (da Costa Filho et al., 2014). Based on the latter approach, an elastic Marchenko imaging method has been proposed (da Costa Filho et al., 2015). All of the above redatuming methods are under the assumption that surface-related multiples are eliminated in the data. To bypass the need to apply surface-related multiple elimination (SRME) to the data, Singh et al. (2015) show a method to directly handle the free surface multiples by adding an extra integral that represents the free surface effect in the Marchenko equations (Singh et al., 2015). Dukalski and de Vos (2017) show that the convergence of the algorithm proposed by Singh et al. (2015) is not always guaranteed. They analytically derive the conditions in which the algorithm proposed by Singh et al. (2015) diverges and present two alternative methods to solve the Marchenko equation, least-squares and a modified Levinson-type algorithm, which do not suffer from the divergence problems but require an increased computational cost. Provided dual-sensor (e.g., pressure and vertical particle velocity) data, Ravasi (2017) and Slob and Wapenaar (2017) propose the methods to solve the couple Marchenko equations that can handle band-limited seismic date with an unknown wavelet from a more flexible acquisition system (arbitrarily located sources above a line of regularly sampled receivers), with free-surface multiples included.

For field data applications, target-oriented Marchenko imaging has been applied to an ocean-bottom cable survey recorded over the Volve North Sea field (Ravasi et al., 2016), and an adaptive Marchenko imaging scheme has been applied to a marine streamer data set (Staring et al., 2017). The application to the Volve field data set presents some encouraging results, as the image produced by Marchenko imaging is more continuous compared with a standard RTM image. Moreover, Marchenko imaging reveals some structural features that are not present in the surface RTM image.

In this paper, we will demonstrate a successful application of Marchenko redatuming and imaging to a marine streamer data set acquired over a salt structure at the Gulf of Mexico. With a salt body, this data set provides sufficient complexities to test the Marchenko redatuming and imaging methods. In a standard marine towed-streamer survey, the near-offset data cannot be recorded and the data contain only one-sided offsets. Hence, we will first perform a set of synthetic experiments to investigate whether the data acquired with such geometry satisfy the requirement for the reflection response of Marchenko redatuming. Then, we will present a workflow (starting from the processing of the raw field data) to produce a subsalt Marchenko image. We will review all the steps in the working flow: processing the raw data, estimating the direct arrival, redatuming through the Marchenko iteration scheme, and imaging using the deconvolution imaging condition. Finally, we will analyze the subsalt Marchenko image and compare it with a standard RTM image created with the same input data set and discuss the improvements gained in the Marchenko image.

METHODOLOGY

In this section, we outline the methodology for the Marchenko framework, including receiver redatuming, source redatuming, and imaging. We focus on the implementation and physical interpretation of receiver redatuming, and we briefly discuss the source redatuming and imaging algorithms used in our application. Readers who do not want the details of the mathematical derivations for receiver redatuming can treat the Marchenko redatuming process as a black box. Given a background velocity model and the surface seismic reflection response, the black box accurately produces the seismic wavefield recorded at a predefined subsurface point (responding to the surface sources) with primary and multiple reflections. In other words, the black box retrieves a virtual vertical seismic profile as if a virtual receiver was placed inside the medium and recorded data due to sources at the surface. Moreover, the retrieved wavefield is decomposed into two components: the upgoing component, which contains the energy that is propagating upward when it arrives at the virtual receiver, and the downgoing component, which contains the energy that is propagating downward when it arrives at the virtual receiver.

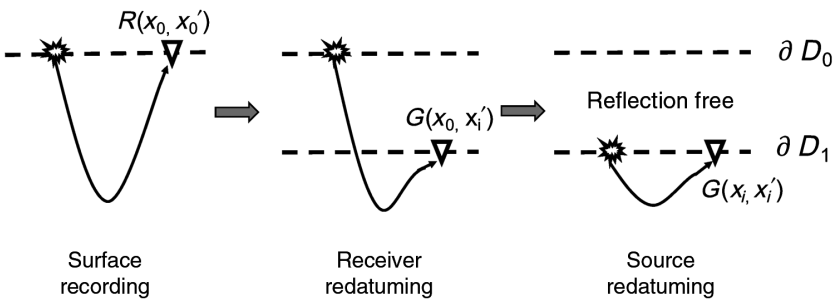

Figure 1. Illustration of the source and receiver levels for surface recording, after receiver redatuming and after source redatuming.

Receiver redatuming

In this study, we use an iterative scheme for receiver redatuming, which is adapted from the work of Broggini et al. (2014) on the basis of the earlier theoretical Marchenko frameworks (Rose, 2002; Broggini et al., 2012; Wapenaar et al., 2014b). The heart of the Marchenko redatuming is the reciprocity theorem. The convolution- and correlation-type reciprocity theorems

relate two wave states with different field, material, and source properties in heterogeneous media (de Hoop, 1988; Wapenaar et al., 2004; Vasconcelos et al., 2009). Source-receiver reciprocity, which states that the same waveform will be observed if the locations of the source and receiver are exchanged, is a special case of the reciprocity theorem.

Figure 2 shows the two wave states that we choose to relate by the reciprocity theorem to derive the Marchenko-type equations. State A is represented by the focusing functions (upgoing component f^- and downgoing component f^+) that are defined in a modified medium that is reflection free below the focusing level ∂D_i. State B is represented by the actual wavefields in the subsurface (upgoing component G^- and downgoing component G^+). In the following discussion, we refer to these physical wavefields as the up- and downgoing Green's functions because the wavefields of state B represent the responses to impulsive point sources. In all our examples, the "Green's functions" shown in the figures are convolved with a Ricker wavelet (15 Hz) for display purposes.

According to the one-way reciprocity theorem, the Green's functions and the focusing functions are related by (Wapenaar et al., 2014b; van der Neut et al., 2015a)

$$\begin{aligned} G^-(x_i,x_0,\omega) &= -f_1^-(x_0,x_i,\omega) \\ &\quad + \int_{\partial D_0} R(x_0,x_0',\omega) f_1^+(x_0',x_i,\omega) dx_0', \\ G^+(x_i,x_0,\omega) &= [f_1^+(x_0,x_i,\omega)]^* \\ &\quad - \int_{\partial D_0} R(x_0,x_0',\omega) [f_1^-(x_0',x_i,\omega)]^* dx_0', \end{aligned} \tag{1}$$

where $G^-(x_i,x_0,\omega)$ and $G^+(x_i,x_0,\omega)$ are the frequency-space domain up- and downgoing Green's functions, with a point source at x_0 at the acquisition surface and a receiver at x_i at a desired subsurface location. The focusing functions $f_1^-(x_0',x_i,\omega)$ and $f_1^+(x_0',x_i,\omega)$ are the up- and downgoing parts of the solution for a specified wave equation whose wavefield focuses at the subsurface location x_i. The term $R(x_0,x_0',\omega)$ contains the earth's reflection response from a vertical dipole source at x_0' (recorded by a pressure receiver at x_0). The left multiplication is equivalent to convolution in the time-space domain, whereas * denotes the complex conjugation.

We solve for $G^-(x_i,x_0,\omega)$ and $G^+(x_i,x_0,\omega)$ by decomposing equation 1 into two time windows: $t < t_d$ and $t > t_d$, where t_d is the direct arrival traveltime from the focusing point x_i to the surface. In the time window when $t < t_d$, the Green's functions $G^+(x_0,x_i,\omega)$ and $G^-(x_0,x_i,\omega)$ are equal to zero. We first decompose f^+ into a direct wave T_d^{inv} and a following coda M^+:

$$\begin{aligned} f_1^+(x_0,x_i,\omega) &= T_d^{\text{inv}}(x_0,x_i,\omega) \\ &\quad + M^+(x_0,x_i,\omega), \end{aligned} \tag{2}$$

and then substitute $f_1^+(x_0,x_i,\omega)$ in equation 1 with equation 2. Then, we compute the focusing functions by the following iterative scheme in the time window $t < t_d$:

$$\begin{aligned} [M_k^+(x_0,x_i,\omega)]^* &= \int_{\partial D_0} R(x_0,x_0',\omega) [f_{1,k}^-(x_0',x_i,\omega)]^* dx_0', \\ f_{1,k+1}^-(x_0,x_i,\omega) &= \int_{\partial D_0} R(x_0,x_0',\omega) M_k^+(x_0',x_i,\omega) dx_0' \\ &\quad + f_{1,0}^-(x_0,x_i,\omega), \end{aligned} \tag{3}$$

with the initial value of f_1^- computed by

$$f_{1,0}^-(x_0,x_i,\omega) = \int_{\partial D_0} R(x_0,x_0',\omega) T_d^{\text{inv}}(x_0',x_i,\omega) dx_0', \tag{4}$$

where T_d^{inv} is the time reversal of the direct arrival from the focusing point to the surface. Note that T_d^{inv} is also the initial value of f_1^+, and T_d^{inv} can be approximated with any approach that can calculate traveltime between two points with a given background velocity model.

Finally, in the time window when $t < t_d$, $G^-(x_i,x_0,\omega)$ and $G^+(x_i,x_0,\omega)$ are obtained by substituting the $f_1^-(x_0',x_i,\omega)$ and $f_1^+(x_0',x_i,\omega)$ into equation 1.

Source redatuming

Once the up- and downgoing Green's functions are correctly retrieved, we use them to obtain the redatumed reflection response $\tilde{R}(x_i,x_i',\omega)$ that satisfies (Wapenaar et al., 2014b)

$$G^+(x_0,x_i,\omega) = \int_{\partial D_i} \tilde{R}(x_i,x_i',\omega) G^-(x_0,x_i',\omega) dx_i'. \tag{5}$$

Here, $\tilde{R}(x_i,x_i',\omega)$ can be interpreted as the redatumed reflection response as if the sources and receivers are placed at depth level ∂D_i in a medium that is identical to the physical medium below ∂D_i and homogeneous above (as shown in the right part of Figure 1). Such redatumed data only contain the seismic reflection events resulting from the geologic structures below ∂D_i. Significantly, any complex overburden between the acquisition depth ∂D_0 and redatumed depth ∂D_i (e.g., weathered layers or salt bodies) does not affect the redatumed data. In this study, we use the MDD approach proposed by van der Neut et al. (2011) and Wapenaar et al. (2014b) to solve equation 5 and obtain $\tilde{R}(x_i,x_i',\omega)$.

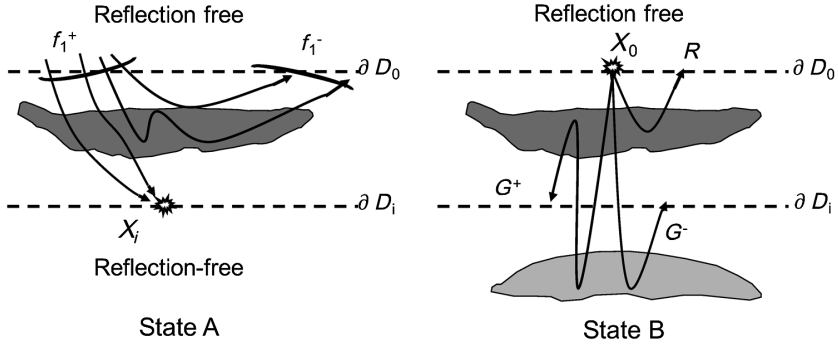

Figure 2. Illustration of the two wavefield states considered in Marchenko redatuming.

Imaging

The redatumed reflection response $\tilde{R}(x_i, x_i', \omega)$ can be used in different ways for imaging. One approach is to obtain the full reflection response by redatuming the sources and receivers at the same depth level and then use the redatumed data to form a seismic image below the redatuming depth level using any established imaging algorithms (e.g., RTM). Note that a velocity model for the areas below the redatuming depth level is also needed in the imaging stage if one wants to perform RTM using the redatumed data in this way.

The following is an alternative approach for imaging (which is the one we adopted in this paper): For every image point inside a target zone, we extract the zero-offset and zero-time component $\tilde{R}(x_i, x_i, t = 0)$ from the redatumed reflection response $\tilde{R}(x_i, x_i', t)$ and we construct an image of the zero-offset reflectivity using

$$I(x_i) = \tilde{R}(x_i, x_i, t = 0). \tag{6}$$

With this imaging condition, we can compute the reflectivity of every image point in a target zone. This approach for imaging is more robust in that it does not create the artifacts from the local internal multiples below the redatuming level, but it comes with an additional cost of performing Marchenko redatuming and MDD for each depth level.

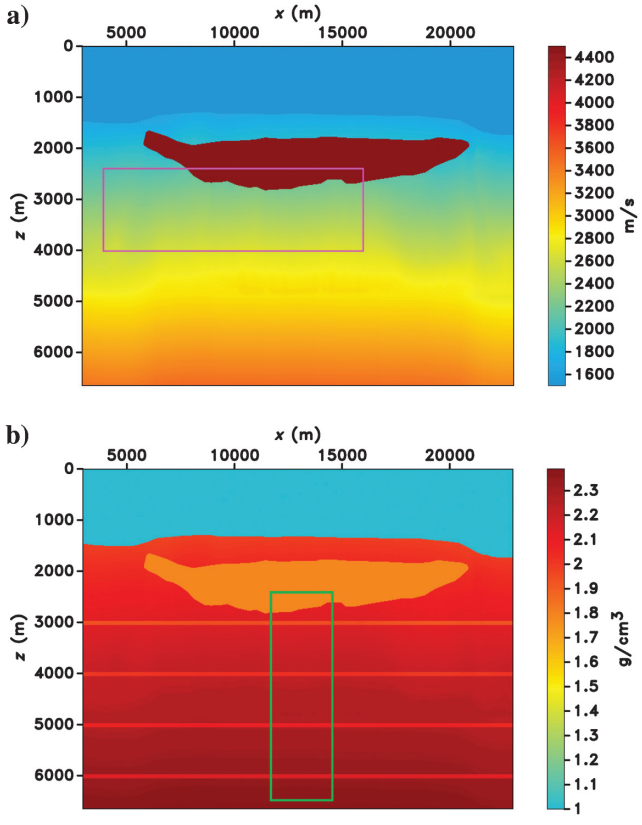

Figure 3. Illustration of the velocity and density models used for the synthetic examples. (a) Velocity model. The red box encloses the target area for which we produce images using field data. (b) Density model. The green box encloses the target area for which we produce images using synthetic data.

SYNTHETIC EXAMPLES

We first demonstrate and interpret the up- and downgoing Green's function retrieved by Marchenko receiver redatuming with a synthetic example for a subsurface point in a 2D acoustic medium (which contains a salt body). We verify the retrieved Green's function by comparing it with the Green's function for the same subsurface point, which is obtained through directly modeling using the finite-difference method. Then, we investigate the influence of the missing near offsets for practical consideration of marine streamer surveys. Finally, we illustrate the importance of calibration for the amplitudes of the data, and we discuss how we calibrate the field data set that we use in the following section.

Green's function obtained through Marchenko redatuming and finite-difference modeling

As a preparation for our field data application, we demonstrate and interpret the up- and downgoing Green's functions retrieved by Marchenko receiver redatuming with a synthetic example. The background velocity model (Figure 3a) is estimated from a Gulf of Mexico (GOM) field data set (the data set that is used in our field data application). In the corresponding density model (Figure 3a and 3b), we add four flat horizontal reflectors with the thickness of 100 m at depth levels of 3, 4, 5, and 6 km. The density of these four reflectors is 100 g/cm^3 smaller than the surrounding areas. We generate 1000 shot records with 361 receivers in each shot record using acoustic finite-difference modeling. The spacing between sources and receivers is set as 26.67 m. This synthetic data set is simulated to match the field data set for the source and receiver locations.

Using Marchenko receiver redatuming, we retrieve the up- and downgoing Green's functions for a subsalt point at $x = 13{,}225$ m and $z = 3500$ m, which is referred to as the virtual receiver. The retrieved downgoing Green's function (Figure 4a) can be interpreted as the seismic wavefields that are excited by the surface sources and are propagating downward when they reach the virtual receiver. The first event (labeled with a) in the downgoing Green's function is the direct arrival from the surface sources to the virtual receiver. The downgoing Green's function contains internal multiples. For example, the hyperbola (labeled with b in Figure 4a) corresponds to the internal multiples that are reflected inside the salt body. The raypath of this event is drawn in Figure 4c, also labeled with b. The retrieved upgoing Green's function (Figure 4b) contains the wavefields that are propagating upward when they reach the virtual receiver. These wavefields start downward propagating from the surface sources and are reflected upward by the structures below the virtual receiver. The three major events in Figure 4b (labeled with 1, 2, and 3) correspond to the primary reflections from the three reflectors below the virtual receiver. Their raypaths are shown in Figure 4c.

The sum of the up- and downgoing Green's functions is the total Green's function recorded at the virtual receiver (Figure 5a). In a numerical experiment to verify the total Green's function retrieved by the Marchenko scheme, we place a line of sources on the surface and a receiver at the same location as the virtual receiver at $x = 13{,}335$ m and $z = 3500$ m and then we record the wavefield directly using finite-difference modeling. As shown in Figure 5, the wavefield retrieved by the Marchenko redatuming method matches very well with the directly modeled wavefield in the near-offset parts. The retrieved Green's function has some artifacts for far

offsets because of the limited acquisition aperture. The inconsistencies in Figure 5 that appear near the direct wave are due to the use of the time reversed direct wave. As demonstrated by Vasconcelos et al. (2015) and Vasconcelos and van der Neut (2016), using a physics-driven estimate of the inverse transmission to obtain the direct arrivals may improve the amplitudes of events in the retrieved Green's functions.

Requirements for acquisition geometry

Marchenko redatuming requires the surface reflection response R to be obtained by an evenly and densely sampled array of sources and receivers with a recording aperture as large as possible. Van der Neut et al. (2015a) show that the sources and receivers should be placed at the corresponding stationary points to retrieve some particular up- or downgoing events, and sometimes stationary points cover the entire surface. The field data set used in this study is acquired with the standard towed-streamer acquisition system, which contains traces on only one side of the source for each shot record. One can reconstruct the traces on the other side of each source using the source-receiver reciprocity theorem, forming a data set with two-sided offsets (given the source line is much longer than the maximum offset). However, the near-offset data cannot be practically acquired for towed marine surveys. In the field data set, we use offsets from $h = -107$ to $h = 107$ m (seven traces) are missing. Therefore, we first investigate whether a data set with missing near offsets in the shot records can be directly used for Marchenko redatuming.

For Marchenko redatuming, each trace in the retrieved Green's functions is constructed by first convolving a trace in the reflection response with a trace in the first arrival, in which both traces correspond to the same location at the surface, and then summing over all of the source locations (equation 1). In our synthetic and field examples, there should be 361 traces in each shot record if the near offsets (including zero offset) can be acquired. With the seven near-offset traces missing in each shot record, each trace in the retrieved Green's functions contains the contribution of the remaining 354 traces. We first consider the moveout time difference Δt between the apex of the hyperbola and the maximum missing near offset in a shot gather to evaluate the influence of these seven missing traces. Under the assumption of horizontally layered earth, Δt is given by

$$\Delta t = \sqrt{t_0^2 + \frac{h^2}{4v_{\mathrm{NMO}}^2}} - t_0, \simeq \frac{h^2}{8v_{\mathrm{NMO}}^2 t_0}, \tag{7}$$

where t_0 is the two-way zero-offset traveltime, h is the maximum missing near offset, and v_{NMO} is the normal moveout velocity. We make a first-order approximation of the square-root term to obtain the formula in equation 7. We are able to obtain a good retrieval of the Green's function from the data with missing near offsets when the variation of the traveltime of the reflection in the missing trace Δt is much less than the dominant wave period of the wave of interest T; hence, we require that

$$\Delta t \lesssim \frac{T}{8}. \tag{8}$$

Spetzler and Snieder (2004) show that the denominator of the right side in equation 8 should be no less than 8/3 for 2D cases and no

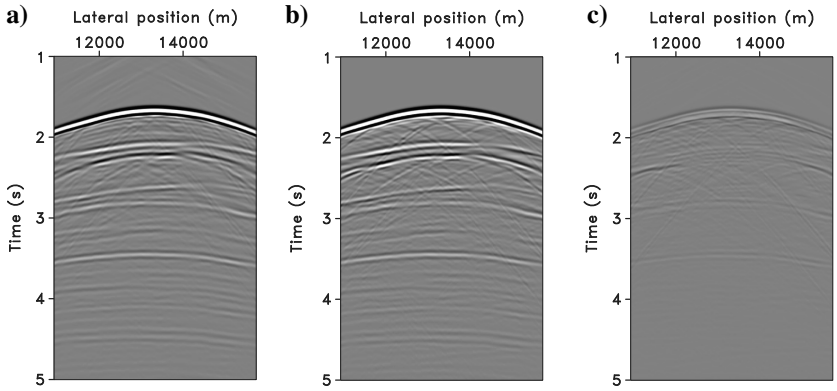

Figure 5. (a) The retrieved the Green's function for a virtual receiver at $x = 13{,}335$ m and $z = 3500$ m.The sum of the up- and downgoing fields of Figure 4. (b) The directly modeled Green's function for a virtual receiver at $x = 13{,}335$ m and $z = 3500$ m. (c) The difference between the retrieved Green's function in (a) and directly modeled Green's function in (b).

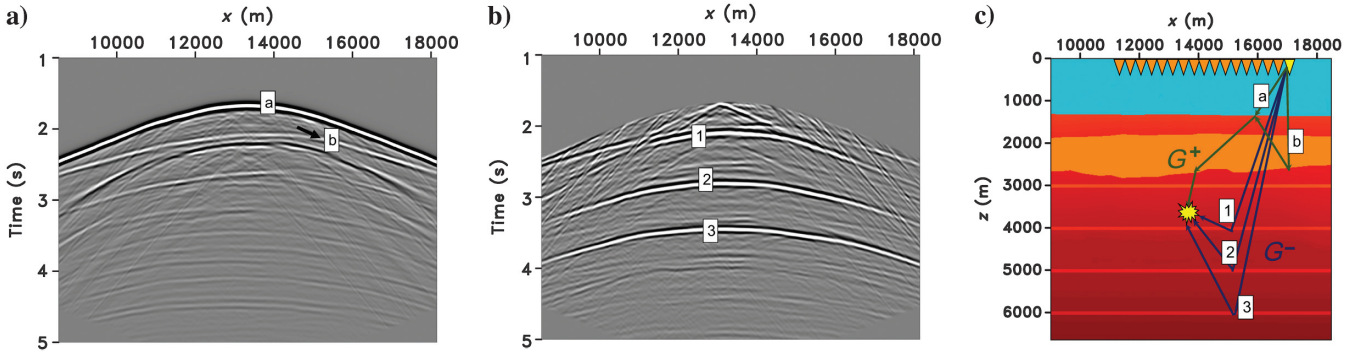

Figure 4. (a) Retrieved downgoing Green's function G^+ and (b) retrieved upgoing Green's function G^-. The linear dipping events appearing approximately 2 s are the artifacts caused by the limited aperture of the data set used in this example. (c) Physical interpretation of G^+ and G^-.

less than 2 for 3D cases (equation 4 in their paper). To be conservative, we use a stricter condition in this derivation and set the denominator of the right side in equation 8 to eight. Then, the maximum missing near offset h should satisfy

$$h \lesssim \sqrt{T v_{\mathrm{NMO}}^2 t_0}, \\ \lesssim \sqrt{2DT v_{\mathrm{NMO}}}, \tag{9}$$

where $D = v_{\mathrm{NMO}} t_0/2$ is the depth of the first interface of interest. Obviously, with fewer missing inner traces (smaller h), we obtain a better retrieval of the Green's functions. Meanwhile, if D, T and v_{NMO} are larger, the Green's function retrieval is less disturbed by the missing near offsets. In a seismic survey, the dominant wave period can be estimated from the frequency spectrum of the data. Equation 9 tells us that the influence of the missing near offsets becomes smaller for deeper events (larger D and v_{NMO}).

To investigate the influence of the missing near offsets numerically, we generate two synthetic data sets using finite-difference modeling with the velocity and density models used above (Figure 3). The first data set (a full data set) contains 361 shot records, with 361 traces in each shot record. For the second data set (a data set with missing near offsets), we remove seven receivers near each source (one trace at the same location as the source position and three nearest traces on both sides), and we obtain the double-sided data set with the maximum missing offset of 214 m (identical to the field data set we use). In this example, D is approximately 1550 m, T is approximately 0.0285 s (as the dominate frequency of the data is approximately 35 Hz), and v_{NMO} is approximately 1500 m/s, so according to equation 9, h should be $\lesssim$258 m. Because the maximum missing offset (214 m) satisfies the criterion (equation 9), we expect a good retrieval of the Green's functions using the data set with missing near offsets. Note that we use a much stricter condition (eight instead of 8/3 in the denominator in equation 8) to account for the fact that the dominant period of the reflection response R can be larger than the data before source deconvolution. This is based on the assumption that the dominant frequency will not increase as many as three times before and after the source deconvolution. The total retrieved Green's functions with the full data set (Figure 6a) and the data set with missing near offsets (Figure 6b) are very close to each other. We show the difference panel of these two Green's functions in Figure 6c. The difference panel shows the effect of the missing near offsets. Some shallow events at the near offset are not fully retrieved using the missing near-offset data, which can be predicted in equation 9. In general, as the internal multiples generators in this example are relatively deep, our approach is not heavily affected by these seven near-offset traces in each shot record.

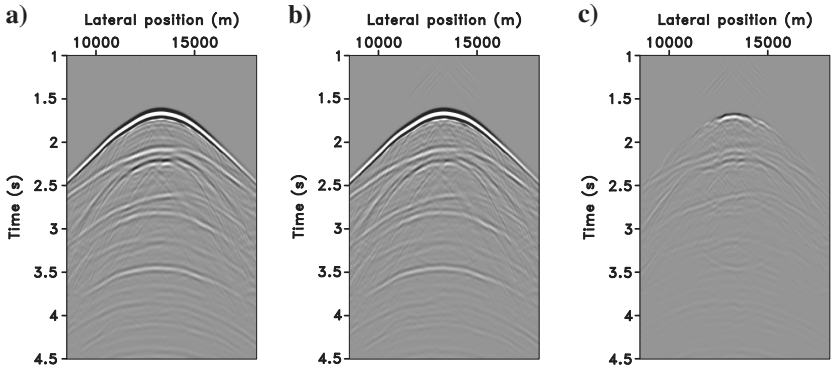

Figure 6. (a) Redatumed field retrieved from the data with full offsets, (b) redatumed field retrieved from the data with missing near offsets, and (c) the difference between (a and b).

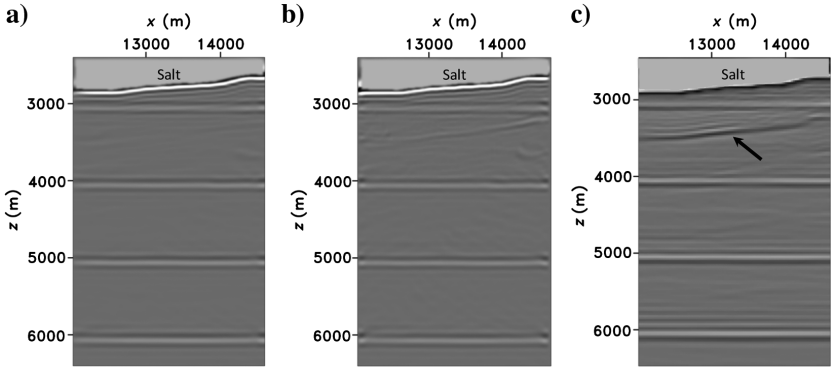

Figure 7. (a) Marchenko image using the data with full offsets, (b) Marchenko image using the data with missing near offsets, and (c) RTM image using the data with full offsets.

We perform Marchenko imaging with the method discussed above for the same target zone (green box in Figure 3b) using these two data sets and apply RTM with the full data set. According to the density model, the final images should contain the salt bottom and four horizontal reflectors. The Marchenko image produced using the full data set (Figure 7a) is very similar to the one produced using the data set with missing near offsets (Figure 7b). Both contain all the expected reflections. Note that in the RTM image (Figure 7c), an additional reflection appears with a similar shape as the salt bottom. This additional reflection is an artifact introduced by a set of pegleg internal multiples. This type of artifact is completely removed in Figure 7a and largely suppressed in Figure 7b. To evaluate the artifact introduced by using the data with missing near offsets, we use the horizontal reflector at $z = 4000$ m as a reference (the maximum amplitude of this reflector is set as 1 unit). The maximum amplitude of the artifact caused by internal multiples (at approximately $x = 13{,}335$ m, $z = 3300$ m) in Figure 7b is 0.52 unit, and the maximum amplitude of the artifact caused by internal multiples (pointed by the black arrow) in Figure 7c is 1.79 unit. Hence, even the artifact is not completely removed when using the data with missing near offsets, the amplitude of the spurious event in the RTM image is approximately 3.5 times larger than that in the Marchenko image produced using the data with missing near offsets. The suppression of the internal multiple artifacts becomes less successful toward the right edge of the image. This may be associ-

ated with the fact that the overlaying salt bottom has a steeper dip on the right side of the image.

Data calibration

The initial step of the iterative scheme in Marchenko redatuming is to convolve the surface reflection response R with the time reversal of the first arrival T_d^{inv} (equation 4). The convolution result is subsequently substituted into equation 3. In the initial iteration of equation 3 ($k = 0$), the convolution result of R and T_d^{inv} is used to convolve with R once more to get M_0^+ and R will be used to convolve with the intermediate results repeatedly in the following iterations. Hence, the amplitudes of the surface reflection response R need to be properly calibrated such that R should be the response to a line of impulsive sources with unit amplitudes. Note, in this example, we obtain the first arrival from a subsurface point to the surface by (1) computing the first-arriving traveltime (using an eikonal solver) and (2) placing a Ricker wavelet (15 Hz) at the first-arriving traveltime. The maximum amplitude of the Ricker wavelet is not significant in the iterative process because it puts a scaling factor on all the Green's functions and focusing functions accordingly (equations 3 and 4), and the scaling factor will drop out during the MDD process indicated in equation 5.

In practice, the first step to approximate the required R from the surface seismic data D is to estimate the source wavelet and deconvolve the source wavelet from D. We then need to calibrate the deconvolved data obtained from the first step by the following approach. In the synthetic examples, we are able to compute the exact scaling factor for data calibration because the source wavelet is known. As shown in Figure 8b, the upgoing Green's function (for a focus point at $x = 13{,}335$ m and $z = 3200$ m) retrieved with the correctly calibrated R is free of artifacts. In Figure 8a and 8c, we show that the retrieved Green's functions are contaminated with artifacts if the data are not correctly calibrated. Figure 8a shows the upgoing Green's function retrieved using the surface reflection response R, which is too small (scaled by a factor of 0.5 relative to the correctly calibrated R). The artifact caused by the incorrect data calibration is depicted in Figure 8a (arrow). When R is too large, the iteration scheme cannot converge. In Figure 8c, we show that when the amplitudes of R are too large (where R is multiplied by a scaling factor of 1.5), the retrieved Green's function is dominated by artifacts. We produce three Marchenko images using the Green's functions retrieved from these three sets of surface reflection responses R: the over-calibrated (with a scaling factor equal to 0.5), the correctly calibrated (with a scaling factor equal to 1), and the under-calibrated (with a scaling factor equals to 1.5). For the over-calibrated case, the artifacts in the Green's functions result in an artifact in the final image (Figure 9a). Note that this artifact shares the shape of the salt bottom and results from an incorrect handling of the internal multiples. For the under-calibrated case, the imaging result completely breaks down (Figure 9c) as the retrieved Green's functions are dominated by artifacts. Finally, in Figure 9b, with the Green's functions retrieved from the correctly calibrated R, we produce an image that is consistent with the velocity and density models and free of artifacts due to multiples.

In the field data application that follows, we obtain the time reversal of the first arrival T_d^{inv} in an exact same way by using the same velocity model to compute the first-arrival time and placing a same Ricker wavelet. However, given a surface seismic data set, we do not have any information about the amplitude of the original source functions. In addition, we do not know what seismic processing steps (e.g., noise attenuation and gain function) the field data set has gone through; hence, the recorded amplitude differs in general from the true amplitude. Therefore, we calibrate the field data set by comparing it with the synthetic data set with missing near offsets (which is used in retrieving the Green's function in Figure 8b). At the same source location, we pick a shot record from the field data set and a shot record from the synthetic data set. By dividing the maximum amplitude of each shot record, we can obtain the scaling factors for the calibration of each field shot record. Different from our method to do amplitude calibration, van der Neut et al. (2015b) use a different approach to estimate the scaling factors.

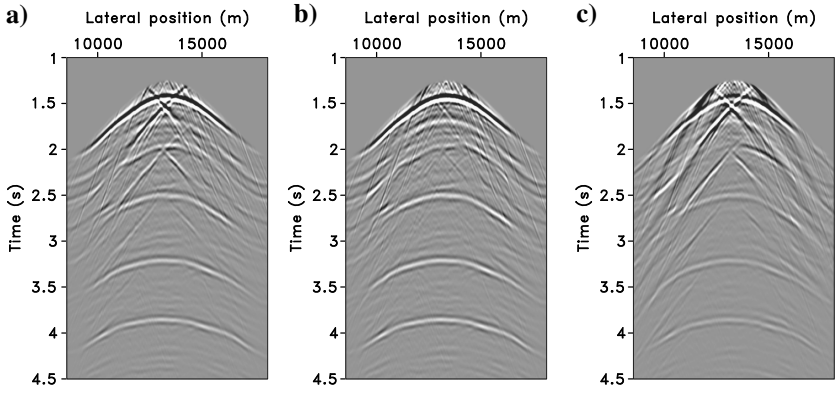

Figure 8. (a) The retrieved upgoing Green's function when the reflection response is scaled by a factor of 0.5. (b) The retrieved upgoing Green's function when the reflection response is scaled by a factor of 1.0. (c) The retrieved upgoing Green's function when the reflection response is scaled by a factor of 1.5.

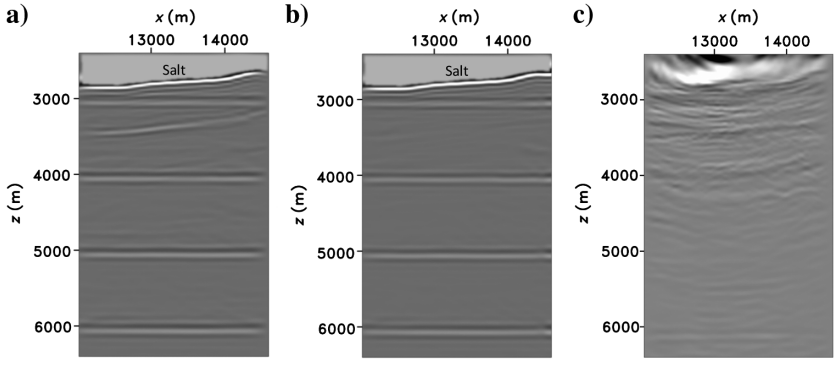

Figure 9. (a) The Marchenko image obtained from the Green's functions retrieved with the reflection response scaled by a factor of 0.5. (b) The Marchenko image obtained from the Green's functions retrieved with the reflection response scaled by a factor of 1.0. (c) The Marchenko image obtained from the Green's functions retrieved with the reflection response scaled by a factor of 1.5.

They apply minimization of the energy norm of the upgoing Green's function as a criterion to perform the data calibration.

FIELD DATA EXAMPLE: MISSISSIPPI CANYON, GULF OF MEXICO

The 2D marine field data set we use was acquired over the Mississippi Canyon in the Gulf of Mexico. This area contains a shallow salt body in a deepwater environment. A total of 1000 shots were fired along a 26 km source line with shot spacing of 26.67 m.

Data processing

In this study, we design a workflow to apply Marchenko imaging to the streamer data set (Figure 10). With a background velocity model, we estimate the direct arrivals from all the subsurface points in the target zone to the surface by computing the traveltime using an eikonal solver using fast marching method (Fomel, 1997) and placing a Ricker wavelet at the direct arrival time. For the data processing, we (1) apply SRME to the surface seismic data for the suppression of the surface multiples, (2) deconvolve the source signature and suppress its bubbles, (3) generate the data with two-sided offsets in the common-shot gathers based on the data with one-sided offsets, and (4) calibrate the amplitudes of the data using the scaling factor estimated from the comparison with the numerically modeled shot records. Details for data preparation are discussed below.

For this data set, the sources and receivers share the same the location along the 2D acquisition line. Note that the colocated sources and receivers are required by Marchenko redatuming; however, shot-based algorithms, such as RTM, do not have such requirements. This field data set has been processed to correct for attenuation. If strong attenuation presents in the data, correction for attenuation is required before applying Marchenko receiver redatuming. Considering that convergence of the approach proposed by Singh et al. (2015) is not always guaranteed, in this study, we start by applying SRME to suppress the free-surface multiples before performing Marchenko redatuming. As shown in equation 3, in the frequency domain implementation of the algorithm, the reflection response $R(\omega)$ is required, not $R(\omega)S(\omega)$ (where the source wavelet is contained in the reflection response). Therefore, the Marchenko redatuming algorithm requires an accurate deconvolution of the source wavelet from the data. We remove the effect of the source signature from the data using the sparse log-domain deconvolution approach of Guitton and Claerbout (2015). Using the reciprocity theorem, we then generate the data with two-sided offsets from the data with one-sided offsets to increase the range of the aperture of the surface reflection response. Theoretically, Marchenko redatuming requires the reflection response to be obtained from dipole sources and pressure receivers (or monopole sources to particle velocity receivers). However, the data set we have is obtained with a pressure source and pressure receivers (standard marine streamer data) and we did not apply any monopole-to-dipole conversion. In this example, even though we discard the requirement for dipole sources and pressure receivers, we are still able to see that the artifacts caused by internal multiples are suppressed in the field Marchenko image (as shown in the "Field data Marchenko images" section); however, the impact of this requirement needs further investigation. As discussed above, we do not need to reconstruct the missing near offsets for this data set. To approximate the physical earth's reflection response R_{real}, after processing the recorded surface data, we also need to calibrate R with a scaling factor s such that $R * s = R_{\text{real}}$. Here, s is an unknown factor that depends on the acquisition methods and the processing chain. In this application, we find this scaling factor by comparing the maximum amplitude of a field shot record with a synthetic shot record because we use the same velocity model and approach to estimate the direct arrivals in synthetic and field data examples. Figure 11 shows the comparison of a field shot record and a synthetic shot record. Because the first waves of both records (which are used to compute the scaling factor) match fairly well, it is reasonable to use the maximum amplitude of the first waves for amplitude calibration. Scaling

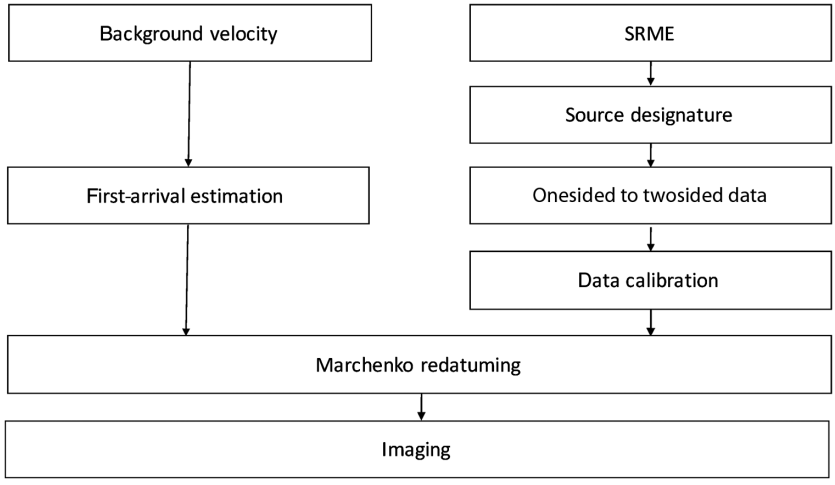

Figure 10. Workflow to apply Marchenko imaging to field data.

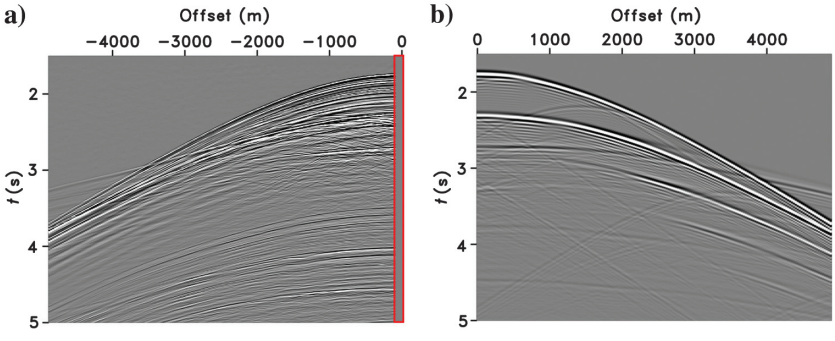

Figure 11. Comparison of (a) field shot record and (b) synthetic shot record that are used to compute the scaling factor. The red box indicates the missing near-offset traces in the field shot record. Note the events due to the three horizontal layers in Figure 3b are included in the synthetic shot record.

factors are computed and applied shot by shot; however, in this example, we find that the scaling factors for all shots do not significantly vary. The approach that we proposed to find the scaling factor is simple and robust, yet one obstacle of this approach is that as we obtain the scaling factor based on the first waves, the rest of the data may be scaled with artifacts. The adaptive Marchenko redatuming method proposed by van der Neut et al. (2015b) is another valid method to overcome the unknown scaling factor issue in the reflection data. Figures 12 and 13 show the comparison of a near-offset section and a shot gather of the raw data and the data after source designature and SRME.

Field data Marchenko images

For imaging, we retrieve the up- and downgoing Green's functions for all of the subsurface imaging points inside the target zone (the red box in Figure 3a, 4.0–16.0 km horizontally and 2.4–4.0 km vertically). We use 11 iterations in the Marchenko redatuming process. The virtual source (focusing points) sampling in the x- and z-directions is 26.67 m, which is the same as the source and receiver sampling on the surface. This target area contains the bottom and the left edge of the salt body, some sediment layers to the left of the salt body, and structures below the salt body. Following equation 5, we create the redatumed reflection response $\tilde{R}(x_i, x_i', \omega)$ at each depth level. Then, we produce the Marchenko image by extracting the zero-time zero-offset value $\tilde{R}(x_i, x_i, t = 0)$, as instructed in equation 6.

A comparison between the Marchenko image (Figure 14b) and the image produced using standard RTM (Figure 14a) shows that they are comparable for the most part: Both present similar structures for the bottom of the salt body, the structures of the sediment layers to the left of the salt body, and the detailed structures of the subsalt area. Furthermore, we find significant improvements in the Marchenko image: (1) The reflectors are more continuous and smoother (the green arrows in Figure 14a and 14b), (2) the structures of the sediment layers to the left of the salt body are more clearly revealed (the red arrows in Figure 14a and 14b), and (3) additional structural features are revealed (the blue arrows in Figure 14a and 14b).

To better understand these improvements accomplished in the Marchenko image, we produce an RTM image for the same target area using the synthetic data set generated using the models in Figure 3. In this RTM image (Figure 14c), we observe some artificial reflections that have a shape similar to the bottom of the salt (the

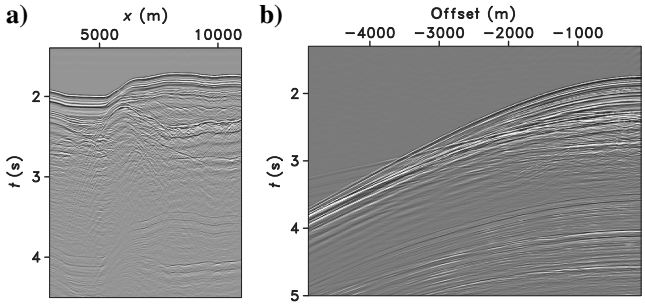

Figure 12. (a) Raw field data: a near-offset section. (b) Raw field data: a shot record.

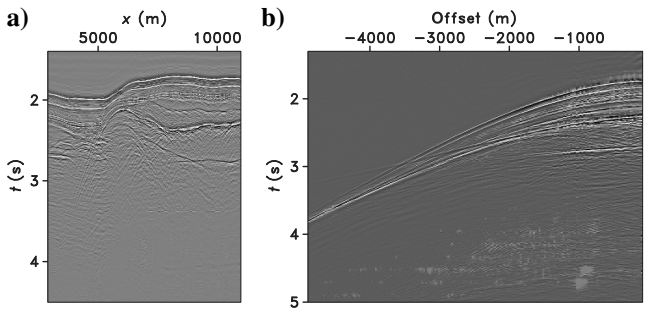

Figure 13. (a) Field data after source designature and SRME: a near-offset section. (b) Field data after source designature and SRME: a shot record.

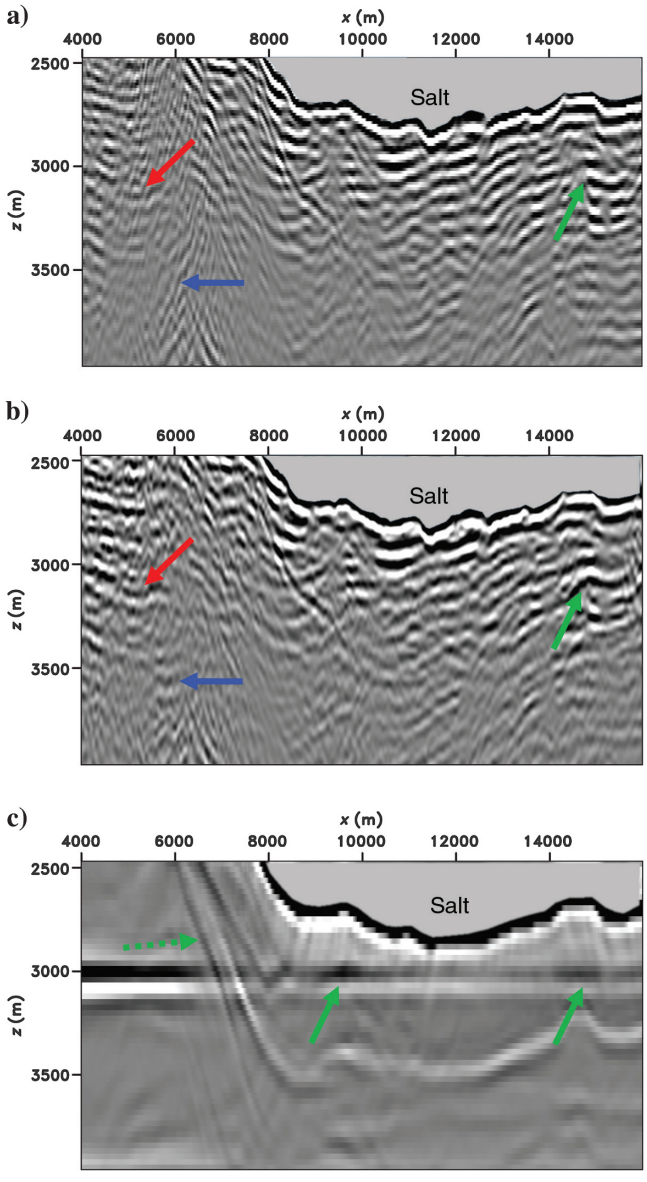

Figure 14. (a) The RTM image with the field data set, (b) Marchenko image with the field data set, and (c) RTM image with the synthetic data set generated from velocity and density models in Figure 3.

dashed green arrow in Figure 14c), which indicates that the artifacts result from internal multiple reflections at the salt bottom. When these artificial structures interfere with the horizontal reflector at 3 km, the phases of the horizontal reflector are either added or subtracted, creating amplitude discontinuities (the solid green arrows in Figure 14c). Hence, the discontinuities in the field data RTM image (Figure 14a) could also result from the interference between the multiple artifacts and the real sedimentary layers. Because the Marchenko imaging method correctly handles internal multiples, it is able to produce an image (Figure 14b) that is more continuous and free from multiple artifacts. The layered structures to the left of the salt body (the red arrows in Figure 14a and 14b), revealed in the RTM image and in the Marchenko image, are sedimentary layers beneath the seabed. Note that the amplitudes of these sedimentary layers in the RTM image are suppressed, whereas the layers are more clearly revealed and more comprehensible in the Marchenko image (the red arrows in Figure 14a and 14b). This is because the imaging approach that we adopted also removes all the artifacts caused by the internal multiples that originate within the target zone (in contrast to the approach of using the MDD-redatumed reflection response as input for RTM). Moreover, Marchenko imaging reveals some structural features (the blue arrows in Figure 14b) that are not presented in the RTM image.

DISCUSSION

Internal multiples can play two completely different roles in seismic imaging: If the primaries are well-recorded, internal multiples create artifacts in migration and therefore should be removed; if there is a significant portion of primaries unrecorded, internal multiples have the potential to improve the illumination of the subsurface and should be used for imaging. In the synthetic and field examples presented in this study, we focus on the artifacts caused by the internal multiples related to salt bodies. In these examples, we assume that the primaries are well-recorded and are sufficient for producing a subsalt image; however, the internal multiples in the data will introduce artifacts that contaminate the image. Wapenaar et al. (2016) discuss the role of multiples in Marchenko imaging and present a potential approach to use multiples (instead of remove) in Marchenko imaging. In our implementation of Marchenko deconvolution imaging, the effect of internal multiples is eliminated for a cleaner subsalt image.

Regarding the value of the denominator on the right side in equation 8, it is set as eight in this study, based on the assumption that the dominant frequency will not increase as many as three times before and after the source deconvolution. Theoretically, it should be larger than 8/3 for 2D cases and larger than 2 for 3D cases (Spetzler and Snieder, 2004). The reason that we use a much stricter value is that the dominant frequency of the reflection response can be larger than the dominant frequency of the original data (before source deconvolution), and a stricter condition will compensate this.

CONCLUSION

We successfully apply subsalt Marchenko redatuming and imaging to a marine data set from the Gulf of Mexico. With some numerical experiments, we investigate the effect of the missing near-offset traces, and we conclude that the artifacts caused by multiples can be largely suppressed by directly using the missing near-offset data. We show that calibration of the data needs to be properly performed, and we calibrate the data based on the comparison with the numerically modeled data set in this study.

We represent that the image produced by Marchenko imaging is more continuous than the RTM image produced using the same data set and velocity model. Furthermore, the Marchenko method seems able to reveal some structures that cannot be found in the RTM image. We use an RTM image produced with a synthetic data set to demonstrate that the discontinuities in the RTM image are very likely caused by internal multiples. The improvements in the Marchenko image over the RTM image demonstrate that for field data, the Marchenko framework is applicable and effective in suppressing the artifacts caused by internal multiples.

ACKNOWLEDGMENTS

We appreciate the enlightening comments of A. Cheng, J. van der Neut, M. Ravasi, F. Broggini, and an anonymous reviewer. We thank the sponsors of the Center for Wave Phenomena, whose support made this research possible. The reproducible numeric examples in this paper use the Madagascar open-source software package freely available from http://www.ahay.org.

REFERENCES

Bakulin, A., and R. Calvert, 2006, The virtual source method: Theory and case study: Geophysics, **71**, no. 4, SI139–SI150, doi: 10.1190/1.2216190.
Berryhill, J. R., 1979, Wave equation datuming: Geophysics, **44**, 1329–1344, doi: 10.1190/1.1441010.
Berryhill, J. R., 1984, Wave equation datuming before stack: Geophysics, **49**, 2064–2066, doi: 10.1190/1.1441620.
Broggini, F., and R. Snieder, 2012, Connection of scattering principles: A visual and mathematical tour: European Journal of Physics, **33**, 593–613, doi: 10.1088/0143-0807/33/3/593.
Broggini, F., R. Snieder, and K. Wapenaar, 2012, Focusing the wavefield inside an unknown 1D medium: Beyond seismic interferometry: Geophysics, **77**, no. 5, A25–A28, doi: 10.1190/geo2012-0060.1.
Broggini, F., R. Snieder, and K. Wapenaar, 2014, Data-driven wavefield focusing and imaging with multidimensional deconvolution: Numerical examples for reflection data with internal multiples: Geophysics, **79**, no. 3, WA107–WA115, doi: 10.1190/geo2013-0307.1.
da Costa Filho, C. A., M. Ravasi, and A. Curtis, 2015, Elastic p-and s-wave autofocus imaging with primaries and internal multiples: Geophysics, **80**, no. 5, S187–S202, doi: 10.1190/geo2014-0512.1.
da Costa Filho, C. A., M. Ravasi, A. Curtis, and G. A. Meles, 2014, Elastodynamic Green's function retrieval through single-sided Marchenko inverse scattering: Physical Review E, **90**, 063201, doi: 10.1103/PhysRevE.90.063201.
de Hoop, A. T., 1988, Time-domain reciprocity theorems for acoustic wave fields in fluids with relaxation: The Journal of the Acoustical Society of America, **84**, 1877–1882, doi: 10.1121/1.397152.
Dukalski, M., and K. de Vos, 2017, Marchenko inversion in a strong scattering regime including surface-related multiples: Geophysical Journal International, **212**, 760–776.
Fomel, S., 1997, A variational formulation of the fast marching eikonal solver: Stanford Exploration Project, SEP-95, 127–147.
Guitton, A., and J. Claerbout, 2015, Nonminimum phase deconvolution in the log domain: A sparse inversion approach: Geophysics, **80**, no. 6, WD11–WD18, doi: 10.1190/geo2015-0016.1.
Kinneging, N., V. Budejicky, C. Wapenaar, and A. Berkhout, 1989, Efficient 2D and 3D shot record redatuming: Geophysical Prospecting, **37**, 493–530, doi: 10.1111/j.1365-2478.1989.tb02220.x.
Ravasi, M., 2017, Rayleigh-Marchenko redatuming for target-oriented, true-amplitude imaging: Geophysics, **82**, no. 6, S439–S452, doi: 10.1190/geo2017-0262.1.
Ravasi, M., I. Vasconcelos, A. Kritski, A. Curtis, C. A. d. C. Filho, and G. A. Meles, 2016, Target-oriented Marchenko imaging of a North Sea field: Geophysical Journal International, **205**, 99–104, doi: 10.1093/gji/ggv528.
Rose, J. H., 2002, Single-sided autofocusing of sound in layered materials: Inverse Problems, **18**, 1923–1934, doi: 10.1088/0266-5611/18/6/329.
Singh, S., R. Snieder, J. Behura, J. van der Neut, K. Wapenaar, and E. Slob, 2015, Marchenko imaging: Imaging with primaries, internal multiples, and free-surface multiples: Geophysics, **80**, no. 5, S165–S174, doi: 10.1190/geo2014-0494.1.

Slob, E., and K. Wapenaar, 2017, Theory for Marchenko imaging of marine seismic data with free surface multiple elimination: 79th Annual International Conference and Exhibition, EAGE, Extended Abstracts, doi: 10.3997/2214-4609.201700800.

Snieder, R., K. Wapenaar, and K. Larner, 2006, Spurious multiples in seismic interferometry of primaries: Geophysics, **71**, no. 4, SI111–SI124, doi: 10.1190/1.2211507.

Spetzler, J., and R. Snieder, 2004, The Fresnel volume and transmitted waves: Geophysics, **69**, 653–663, doi: 10.1190/1.1759451.

Staring, M., R. Pereira, H. Douma, J. van der Neut, and C. Wapenaar, 2017, Adaptive double-focusing method for source-receiver Marchenko redatuming on field data: 87th Annual International Meeting, SEG, Expanded Abstracts, 4808–4812.

van der Neut, J., J. Thorbecke, K. Mehta, E. Slob, and K. Wapenaar, 2011, Controlled-source interferometric redatuming by crosscorrelation and multidimensional deconvolution in elastic media: Geophysics, **76**, no. 4, SA63–SA76, doi: 10.1190/1.3580633.

van der Neut, J., I. Vasconcelos, and K. Wapenaar, 2015a, On Green's function retrieval by iterative substitution of the coupled Marchenko equations: Geophysical Journal International, **203**, 792–813, doi: 10.1093/gji/ggv330.

van der Neut, J., K. Wapenaar, J. Thorbecke, and E. Slob, 2015b, Practical challenges in adaptive Marchenko imaging: 85th Annual International Meeting, SEG, Expanded Abstracts, 4505–4509.

Vasconcelos, I., R. Snieder, and H. Douma, 2009, Representation theorems and Green's function retrieval for scattering in acoustic media: Physical Review E, **80**, 036605, doi: 10.1103/PhysRevE.80.036605.

Vasconcelos, I., and J. van der Neut, 2016, Full-wavefield redatuming of perturbed fields with the Marchenko method: 78th Annual International Conference and Exhibition, EAGE, Extended Abstracts, doi: 10.3997/2214-4609.201600624.

Vasconcelos, I., K. Wapenaar, J. van der Neut, C. Thomson, and M. Ravasi, 2015, Using inverse transmission matrices for Marchenko redatuming in highly complex media: 85th Annual International Meeting, SEG, Expanded Abstracts, 5081–5086.

Wapenaar, K., 2014, Single-sided Marchenko focusing of compressional and shear waves: Physical Review E, **90**, 063202, doi: 10.1103/PhysRevE.90.063202.

Wapenaar, K., J. Thorbecke, and D. Draganov, 2004, Relations between reflection and transmission responses of three-dimensional inhomogeneous media: Geophysical Journal International, **156**, 179–194, doi: 10.1111/j.1365-246X.2003.02152.x.

Wapenaar, K., J. Thorbecke, J. van der Neut, F. Broggini, E. Slob, and R. Snieder, 2014a, Green's function retrieval from reflection data, in absence of a receiver at the virtual source position: The Journal of the Acoustical Society of America, **135**, 2847–2861, doi: 10.1121/1.4869083.

Wapenaar, K., J. Thorbecke, J. van der Neut, F. Broggini, E. Slob, and R. Snieder, 2014b, Marchenko imaging: Geophysics, **79**, no. 3, WA39–WA57, doi: 10.1190/geo2013-0302.1.

Wapenaar, K., J. van der Neut, and E. Slob, 2016, On the role of multiples in Marchenko imaging: Geophysics, **82**, no. 1, A1–A5, doi: 10.1190/geo2016-0323.1.